7 Raman Scattering

When a new material is discovered – or a long-known material suddenly turns out to be of great physical interest – Raman spectroscopy is usually among the first experimental techniques used for characterization. Spectra can be recorded on small and little-known samples, and provide deep insight into the physical properties as well as the material quality. During the last decade Raman spectrometers have become rather cheap and easy to handle, in particular, the single-grating spectrometers working with a notch filter. The Raman process yields information not only on the vibrational properties. Resonant scattering is deeply influenced by the electronic states of a system, phase transitions are nicely studied by recording the Raman spectra, and experiments under external pressure allow us to understand the elastic properties as well.

In this chapter we briefly discuss the basics of Raman scattering (Sect. 7.1) in as much as they are important for the analysis of carbon nanotube spectra. For newly discovered materials without single-crystal quality – such as carbon nanotubes for the time being – one of the interesting questions is what the symmetry of observed modes is. We show in Sect. 7.2 how such a symmetry analysis can be performed on unoriented samples. In Sect. 7.3 we discuss how information at large wave vectors can be obtained with Raman scattering. We will pay attention to resonance phenomena, focusing on the Raman double resonance (Sect. 7.4), which has become a central subject in the understanding of Raman scattering in graphite and carbon nanotubes.

7.1 Raman Basics and Selection Rules

First-order Raman scattering is a three-step process as shown in Fig. 7.1. The absorption of an incoming photon with a frequency ω_1 creates an electron–hole pair, which then scatters inelastically under the emission of a phonon with frequency ω_{ph}, and finally recombines and emits the scattered photon ω_2.[7.1],[7.2] Energy and momentum are conserved in the Raman process

$$\hbar\omega_1 = \hbar\omega_2 \pm \hbar\omega_{ph} \tag{7.1}$$

$$\boldsymbol{q}_1 = \boldsymbol{q}_2 \pm \boldsymbol{q}_{ph}, \tag{7.2}$$

where the $\pm$ signs refer to Stokes and anti-Stokes scattering. The details of the electron–photon and the electron–phonon coupling are included in the corresponding matrix elements. Let the polarization of the incoming (outgoing) light be σ (ρ) and the Hamiltonian for electron–radiation interaction $H_{eR,\sigma}$ ($H_{eR,\rho}$); the electron–phonon coupling is given by H_{ep}. The matrix

Figure 7.1: Feynman diagram of a first-order Raman process. An incoming photon with frequency ω_1 and wave vector k_1 excites an electron hole pair. The electron is scattered inelastically emitting a phonon with frequency ω and wave vector q. The electron–hole pair recombines under the emission of the scattered photon (k_2, ω_2). After Ref. [7.1].
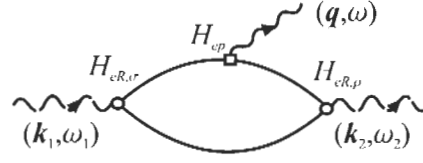
element $K_{2f,10}$ of the process in Fig. 7.1 is then[7.3]

$$K_{2f,10} = \sum_{a,b} \frac{\langle \omega_2, f, i | H_{eR,\rho} | 0, f, b \rangle \langle 0, f, b | H_{ep} | 0, 0, a \rangle \langle 0, 0, a | H_{eR,\sigma} | \omega_1, 0, i \rangle}{(E_1 - E_{ai}^e - i\gamma)(E_1 - \hbar\omega - E_{bi}^e - i\gamma)},$$

(7.3)

where $| \omega_1, 0, i \rangle$ denotes the state with an incoming photon of energy $E_1 = \hbar\omega_1$, the ground state 0 of the phonon (no phonon excited), and the ground electronic state i; the other states are labeled accordingly. The initial and final electronic states are assumed to be the same; the sum is over all possible intermediate electronic states a and b. The final phononic state is denoted by f. The E_{ai}^e are the energy differences between the electronic states a and i; the lifetime of the excited states γ is taken to be the same.

The Raman intensity is proportional to the square of $|K_{2f,10}|$ in Eq. (7.3) and difficult to evaluate, because the matrix elements are usually not known. For a calculation of the resonant spectrum it is common to take the numerator to be constant and integrate over possible intermediate states a and b as described, e.g., in Ref. [7.3]. For the double-resonance process another matrix element and a further resonant term in the denominator is included, see Sect. 7.4. In a single (or double) resonance the Raman cross section

$$I \sim |K_{2f,10}|^2$$

(7.4)

diverges when the intermediate states a or b are real and one (or several) terms in the denominator of Eq. (7.3) vanish. The lifetime γ keeps the Raman cross section finite.

When interested only in selection rules the question is whether the matrix element in Eq. (7.3) is zero or not. The quickest way to work out the selection rules for Raman scattering in carbon nanotubes is to use the conservation of the quasi-angular momentum m and the parity σ_h (the latter only for achiral tubes). Treating m as a conserved quantum number implicitly assumes that no *Umklapp* processes occur in the Raman transition;[7.4] see also Chap. 2. This assumption is correct as long as only first-order scattering with q 0 and optical transitions in the visible ($\Delta k \approx 0$) are taken into account. An extension to more general transitions, in particular in defect-induced scattering,[7.5] will be performed as well.

The eigenstates in Eq. (7.3) are composed of an electronic, a vibronic, and a photonic part. The quantum numbers are conserved for the total eigenstate. Since the initial and final electronic state is the same – excluding vibro-electronic coupling[7.6],[7.7] – $\Delta m = 0$ and $\sigma_h = +1$ for the electronic part. A z-polarized optical transition conserves angular momentum $\Delta m = 0$ and changes the mirror parity $\sigma_h = -1$; for transitions polarized perpendicular to the tube axis $\Delta m = \pm 1$ and $\sigma_h = +1$.[7.8] The change in angular momentum and parity induced by the

Table 7.1: Phonon symmetries conserving the angular momentum quantum number and the σ_h parity in the Raman configurations. In chiral tubes σ_h is not a symmetry operation; the superscript $\pm$ and the subscript g are omitted.

Scattering geometry	Phonon symmetries	
	Line group notation	Molecular notation
(z,z)	$_0A_0^+$	A_{1g}
(x,z), (z,x), (y,z), (z,y)	$_0E_1^-$	E_{1g}
(x,x), (y,y)	$_0A_0^+$, $_0E_2^+$	A_{1g}, E_{2g}
(x,y), (y,x)	$_0B_0^+$, $_0E_2^+$	A_{2g}, E_{2g}

absorption and emission of a photon must be compensated for by the phonon. For z-polarized incoming and outgoing light – (zz) configuration in the usual Raman notation – angular momentum and parity are fully conserved by the photons. Therefore, only $A_0^+ = A_{1g}$ phonons are allowed in this scattering configuration. In (xz) or (zx) scattering geometry $\Delta m_{photon} = \pm 1$ and $\sigma_{h,photon} = -1$ giving rise to E_1^- – E_{1g} phonon scattering. The selection rules for Γ-point phonons are summarized in Table 7.1 for all possible scattering configurations.

Let us now consider the Raman selection rules for scattering with $q \neq 0$, including either defect scattering or a second phonon. Again they can be derived in the standard way from the character table (Table 2.5) of the line group[7.4],[7.9] or found from the conservation of quantum numbers.[1] We will see that phonon branches of carbon nanotubes that are derived from a Raman-active Γ-point mode are always allowed. We assume that a possible defect cannot change the symmetry of a state it interacts with ($m_{defect} = 0$), *i.e.*, it scatters electrons only within the same band. As for scattering with Γ-point modes, the phonon provides the quantum numbers by which the electronic system is changed through the optical transitions in a given scattering geometry, *e.g.*, $\Delta m = m_{ph} \pm 1$ for (x,z) polarization of incoming and outgoing light, respectively. We summarize the required quantum numbers in Table 7.2. The σ_h parity in achiral tubes (given in brackets) is defined only for $q = 0$. The vertical mirror plane (σ_x) is present for $q \neq 0$ if $m = 0$ or $m = n$. From the conservation of the σ_x parity it follows that the entire LO branch (including $q = 0$) is allowed in zig-zag tubes and forbidden in armchair tubes; and *vice versa*, the TO branch is allowed in armchair tubes but forbidden in zig-zag nanotubes. In two-phonon scattering, the change in quantum numbers is provided in total by both phonons, *i.e.*, $\Delta m = m_{ph} = m_{ph,1} + m_{ph,2}$. Therefore, in contrast to first-order scattering, also modes with $|m| > 2$ can contribute to the two-phonon signal. They scatter electrons from one band into another band. The quasi-angular momentum m of the phonon defines to which band the excited electron is scattered through $m_b = m_a + m_{ph}$, where the subscripts a and b refer to the intermediate electronic states, see also Eq. (7.24).

If the phonon wave vector is larger than π/a, the quasi-angular momentum m is not a conserved quantum number and the *Umklapp* rules [Eq. (2.20) and (2.21)] apply. For achiral tubes, $m = 0$ changes into $m = n$ for $q \in (\pi/a, 2\pi/a]$. In chiral tubes, it is more convenient to use the helical quantum numbers $\tilde{k}, \tilde{m}$; then the entire $\tilde{m} = 0$ band is allowed in (z,z) configuration. To summarize, the selection rules for large-q Raman scattering in carbon nanotubes

---

[1]Note that also the quasi-momentum conservation, $q_1 = q_2 \perp q_{ph}$, is found formally from the full space group character table as given in Table 2.5.

Table 7.2: Phonon quantum numbers conserving the total quantum numbers in $q \neq 0$ Raman scattering. The m quantum number m_{ph} refers to scattering by one or more phonons. For two-phonon scattering, $m_{ph} = m_{ph,1} + m_{ph,2}$. If one phonon is replaced by a defect, $m_{ph} = m_{ph,1} + m_{defect} = m_{ph,1}$. The parity quantum numbers given in brackets on the right are only defined at $q = 0$. In chiral tubes σ_h and σ_x are not a symmetry operation.

Scattering geometry	Allowed phonon quantum numbers		
	m_{ph}	$\sigma_{x,ph}$	$\sigma_{h,ph}$
(z,z)	0	$+1$	$(+1)$
$(x,z), (z,x), (y,z), (z,y)$	± 1	$-$	(-1)
$(x,x), (y,y)$	$0; \pm 2$	$+1; -$	$(+1)$
$(x,y), (y,x)$	$0; \pm 2$	$-1; -$	$(+1)$

are given by the conservation of the quasi-angular momentum m. If $q > \pi/a$, the *Umklapp* rules must be additionally applied. For $m = 0$ and $m = n$ phonons in achiral tubes, the allowed modes are further restricted by parity quantum numbers. In general, for $q \neq 0$ the selection rules are less restrictive than for Γ'-point phonons, since some of the parity quantum numbers are defined only at $q = 0$. If a phonon mode is forbidden at the Γ point but allowed for $q > 0$, however, continuity prevents the mode from having a large Raman signal for small q. For an in-depth treatment of the optical transitions, see Chap. 4.

The Raman-scattering intensity I is usually evaluated by contracting the Raman tensors $\mathfrak{R}$

$$I \sim |\boldsymbol{e}_s \cdot \mathfrak{R} \cdot \boldsymbol{e}_i|^2, \tag{7.5}$$

where $\boldsymbol{e}_i$ and $\boldsymbol{e}_s$ are the polarization vectors of incident and scattered light, respectively. The Raman tensors of the modes given in Table 7.1 can be found by the group projector technique introduced in Chap. 2. Often, an inspection of the table together with symmetry arguments is sufficient to find the general form of the Raman tensors. The A_{1g} representation appears only for parallel polarizations, hence all non-diagonal elements of its Raman tensor must be zero. Various symmetry operations transform the xx- and the yy-components into each other in nanotubes. To obtain an A_{1g} representation these two entries of the tensor must be the same. The zz-component, on the other hand, is linearly independent, because all line group symmetry operations preserve the z-axis. We thus obtain $diag[a,a,b]$, *i.e.*, a purely diagonal matrix with $\alpha_{xx} = \alpha_{yy} = a$ and $\alpha_{zz} = b$, see Table 7.3, as the general form of an A_{1g} Raman tensor of single-walled nanotubes. E_{1g} can only have xz, zx, yz, zy non-zero elements. Again xz and yz transform into each other under the symmetry operations of the tubes and are not independent, whereas xz and zx are decoupled. Similarly, the other Raman tensors can be found; they are listed in Table 7.3. The experimentally observed selection rules arise from the zeros in the Raman tensor and, with single crystals of carbon nanotubes at hand, the symmetries of all Raman excitations could be determined. At present, however, such crystals are not available. Samples with a partial alignment along the z-axis or dilute nanotube samples on different substrates have been used for Raman experiments.[7.10]–[7.18]

7.2 Tensor Invariants

When single crystals of a material are not available the symmetries of Raman excitations can be studied by measuring the polarization of the scattered light in unoriented samples. One can thus determine the so-called Raman tensor invariants,[7.19],[7.20] which yield information about the symmetry, although the assignment is not always unique.

Let us assume a phonon with a diagonal Raman tensor with three elements $a_1 \neq a_2 \neq a_3$. Furthermore, the scattering configuration in the laboratory frame is (ZZ). To find the Raman intensity we integrate and average over all possible orientations of the crystal. Using Euler's angles[7.21],[7.22]

$$I_{ZZ} = \frac{1}{8\pi^2} \int_0^{\pi,2\pi,2\pi} |e_i \cdot \Re \cdot e_s|^2 \, d\psi \, d\varphi \sin\vartheta \, d\vartheta \tag{7.6}$$

$$= \frac{1}{8\pi^2} \int_0^{\pi,2\pi,2\pi} \langle \begin{pmatrix} \sin\varphi \sin\vartheta \\ \cos\varphi \sin\vartheta \\ \cos\vartheta \end{pmatrix} \begin{pmatrix} a_1 & & \\ & a_2 & \\ & & a_3 \end{pmatrix} \begin{pmatrix} \sin\varphi \sin\vartheta \\ \cos\varphi \sin\vartheta \\ \cos\vartheta \end{pmatrix} \rangle^2 \, d\psi \, d\varphi \sin\vartheta \, d\vartheta, \tag{7.7}$$

integrating and rearranging yields

$$I_{ZZ} = \frac{45\bar{\alpha}^2 + 4\gamma_s'^2}{45} \tag{7.8}$$

$$\text{with} \quad \bar{\alpha} = \tfrac{1}{3}(a_1 + a_2 + a_3) \tag{7.9}$$

$$\gamma_s'^2 = \tfrac{1}{2}\left[(a_1 - a_2)^2 + (a_2 - a_3)^2 + (a_3 - a_1)^2\right]. \tag{7.10}$$

The result in Eq. (7.8) holds for all parallel polarizations of the incoming and outgoing linearly polarized light and for every Raman tensor except that $\gamma_s'^2$ then has a more general form (see below). For perpendicular linear polarization, *e.g.*, I_{XZ}, the integration yields $I_{XZ} = 3\gamma_s'^2/45$. Now it becomes obvious that the symmetry can also be partially deduced from experiments on unoriented materials. For example, if the three elements of the Raman tensor are the same ($= a$, as for cubic point groups), Raman scattering is forbidden in crossed linear polarization, and in parallel linear polarization we find simply $I_{ZZ} = a^2$ and, thus $I_{XZ}/I_{ZZ} = 0$. On the other hand, a fully uniaxial Raman tensor ($a_1 = a_2 = 0$, $a_3 = b$) results in $I_{XZ}/I_{ZZ} = 1/3$.

In Appendix B we show how to generalize the results of the preceding paragraph for arbitrary Raman tensors. The intensity on unoriented substances follows directly from the

Table 7.3: Raman tensors of the phonons in carbon nanotubes. They are valid for the D_q and D_{qh} point groups with $q > 3$, which refers to all realistic tubes.

$A_{1(g)}$	$A_{2(g)}$	$E_{1(g)}$	$E_{1(g)}$	$E_{2(g)}$	$E_{2(g)}$
$\begin{pmatrix} a & 0 & 0 \\ 0 & a & 0 \\ 0 & 0 & b \end{pmatrix}$	$\begin{pmatrix} 0 & e & 0 \\ -e & 0 & 0 \\ 0 & 0 & 0 \end{pmatrix}$	$\begin{pmatrix} 0 & 0 & c \\ 0 & 0 & 0 \\ d & 0 & 0 \end{pmatrix}$	$\begin{pmatrix} 0 & 0 & 0 \\ 0 & 0 & -c \\ 0 & -d & 0 \end{pmatrix}$	$\begin{pmatrix} 0 & f & 0 \\ f & 0 & 0 \\ 0 & 0 & 0 \end{pmatrix}$	$\begin{pmatrix} -f & 0 & 0 \\ 0 & f & 0 \\ 0 & 0 & 0 \end{pmatrix}$

transformation of a tensor under rotation. A second-rank tensor can be decomposed with respect to the rotation group into a scalar (tensor of rank zero), an antisymmetric matrix (rank one), and a symmetric traceless matrix (rank two). These irreducible components have well-defined quantum numbers and transformation properties under rotation. The matrix element for a fixed orientation is obtained from the Wigner–Eckart theorem; the integration over all crystal orientations is determined by the tensor invariants. Different authors use slightly different invariants in Raman scattering. Following Nestor and Spiro[7.23] we define the isotropic invariant

$$\bar{\alpha} = \tfrac{1}{3}(\alpha_{xx} + \alpha_{yy} + \alpha_{zz}), \tag{7.11}$$

the antisymmetric anisotropy

$$\gamma_{as}^2 = \tfrac{3}{4}\left[(\alpha_{xy} - \alpha_{yx})^2 + (\alpha_{xz} - \alpha_{zx})^2 + (\alpha_{yz} - \alpha_{zy})^2\right], \tag{7.12}$$

and the symmetric anisotropy

$$\gamma_s^2 = \tfrac{1}{2}[(\alpha_{xx} - \alpha_{yy})^2 + (\alpha_{yy} - \alpha_{zz})^2 + (\alpha_{zz} - \alpha_{xx})^2] + \tfrac{3}{4}[(\alpha_{xy} + \alpha_{yx})^2 \\ + (\alpha_{xz} + \alpha_{zx})^2 + (\alpha_{yz} + \alpha_{zy})^2], \tag{7.13}$$

where α_{ij} ($i, j = x, y, z$) are the elements of the Raman matrix as given in Table 7.3 for carbon nanotubes.

The scattering intensity on an unoriented sample in any scattering configuration can be expressed by a linear combination of the tensor invariants, see Appendix B. For linear parallel ($\parallel$) and perpendicular ($\perp$) polarization of the incoming and scattered light the intensities are given by (apart from a constant factor; Table B.2)

$$I_\parallel = 45\bar{\alpha}^2 + 4\gamma_s^2 \tag{7.14}$$

$$I_\perp = 3\gamma_s^2 + 5\gamma_{as}^2, \tag{7.15}$$

which is the generalized result of Eq. (7.8). The quotient $I_\perp/I_\parallel$ is known as the depolarization ratio ρ. Under non-resonant conditions the antisymmetric invariant vanishes, $\gamma_{as}^2 = 0$. Measuring the intensity under parallel and crossed polarization is then sufficient to find the tensor invariants. In resonance, the antisymmetric scattering does not necessarily vanish, and we need at least one more independent measurement to find the tensor invariants. Using circular instead of linear polarization the intensities in backscattering configuration are

$$I_{\circlearrowleft\circlearrowright} = 6\gamma_s^2 \tag{7.16}$$

$$I_{\circlearrowleft\circlearrowleft} = 45\bar{\alpha}^2 + \gamma_s^2 + 5\gamma_{as}^2, \tag{7.17}$$

where $I_{\circlearrowleft\circlearrowleft}$ is the intensity for corotating and $I_{\circlearrowleft\circlearrowright}$ for contrarotating incoming and outgoing light; $I_{\circlearrowleft\circlearrowright}/I_{\circlearrowleft\circlearrowleft}$ is the reversal coefficient P. Solving the system of four equations Eqs. (7.14)–(7.17) with respect to the tensor invariants we obtain as one possible solution[7.23]

$$45\bar{\alpha}^2 = I_\parallel - \tfrac{2}{3}I_{\circlearrowleft\circlearrowright}, \tag{7.18}$$

$$5\gamma_{as}^2 = I_\perp - \tfrac{1}{2}I_{\circlearrowleft\circlearrowright}, \tag{7.19}$$

$$6\gamma_s^2 = I_{\circlearrowleft\circlearrowright}. \tag{7.20}$$

With the last quantity $I_{\circlearrowright\circlearrowleft}$ we can measure the experimental error. The experimentally obtained tensor invariants are only accepted as significantly different from zero if they are larger than $\Delta I = |(I_{\parallel} + I_{\perp}) - (I_{\circlearrowright\circlearrowright} + I_{\circlearrowright\circlearrowleft})|$.

In general, the conclusions that can be drawn from experiments on unoriented samples are as follows: The only symmetry that has a non-vanishing isotropic part $\bar{\alpha}$ is the fully symmetric representation in any point or space group. Thus, phonons of A_1 symmetry are readily distinguished from the other species. Of particular interest is the observation of antisymmetric contributions to the Raman intensity, *i.e.*, $\gamma_{as}^2 \neq 0$. If only the antisymmetric component is present the Raman peak originates from a phonon transforming as the totally antisymmetric representation, in the point group of nanotubes this is A_2 (Table 7.3). Totally antisymmetric scattering is scarcely observed experimentally; more frequent is an antisymmetric contribution to a degenerate mode.[7.23]-[7.25] The only possible modes in nanotubes showing mixed symmetric and antisymmetric scattering are E_1 modes. For example, a strong incoming resonance with an optical transition that is allowed in z-polarization, but forbidden in x- or y-polarization yields in the matrix representation of the E_1 Raman tensor $c \neq d$ (Table 7.3). Such antisymmetric contributions were reported by Rao *et al.*[7.12],[7.26],[7.27] for multiwall nanotubes. Degenerate modes have a symmetric anisotropy γ_s^2 different from zero, but $\bar{\alpha}^2 \approx 0$. A large ratio $\gamma_s^2/\bar{\alpha}^2$ can serve as an indicator for scattering by E_1 and E_2 symmetry modes in carbon nanotubes.

7.2.1 Polarized Measurements

The tensor invariants of the Raman scattered light can be obtained from a linear combination of the intensities in linear and circular polarization as shown in Sect. 7.2. Such a basic setup – a combination of two linear polarizing elements (a Fresnel rhomb and a polarization filter) and a $\lambda/4$ wave plate – is shown in Fig. 7.2. It allows the Raman intensities to be recorded in parallel, perpendicular, corotating, and contrarotating polarization without changing the illumination level or removing any polarizing elements in the light path between the measure-
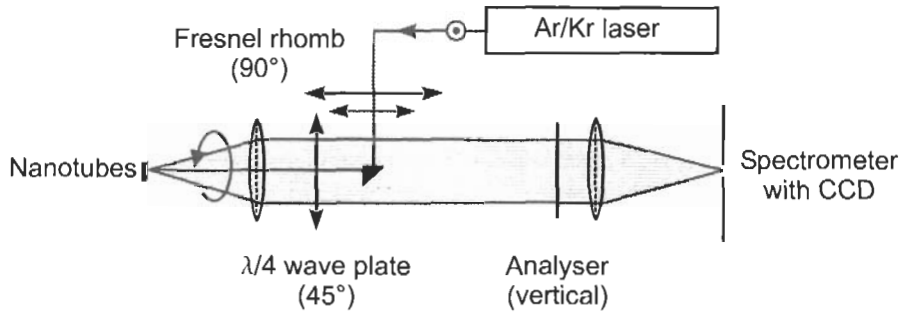

Figure 7.2: Raman setup for the measurements of the tensor invariants. The polarization direction of the incoming light is chosen by the Fresnel rhomb. The laser then passes a $\lambda/4$ zero-order wave plate and is focused onto the sample. The scattered light comes back through the $\lambda/4$ plate, is analyzed with a polarization filter, and focused onto the entrance slits of the spectrometer. Different orientations of the Fresnel rhomb and the $\lambda/4$ plate yield the relative polarizations without inserting additional elements.

Table 7.4: For a fixed spetrometer polarization the settings of Fresnel rhomb and $\lambda/4$ wave plate set up as in Fig. 7.2 allow a recording of the four different relative polarizations of incident and scattered light without inserting or removing an optical element.

Polarization		Fresnel rhomb	$\lambda/4$ plate	Analyzer
Parallel	$I_{\parallel}$	$0°$	$0°$	vertical
Perpendicular	$I_{\perp}$	$90°$	$0°$	vertical
Corotating	$I_{\circlearrowright\circlearrowright}$	$0°$	$45°$	vertical
Contrarotating	$I_{\circlearrowright\circlearrowleft}$	$90°$	$45°$	vertical

ments.[7.19],[7.20],[7.23] We illustrate the arrangement in some more detail since it is relatively unknown; yet it yields the tensor invariants with high accuracy.

For the polarizing elements in positions as indicated in Fig. 7.2 a backscattering Raman spectrum under corotating polarization is recorded: The laser light is vertically polarized and, after passing the Fresnel rhomb ($90°$ position), light is horizontally linearly polarized. After passing the $\lambda/4$ wave plate (its principle axis is at $45°$ to the horizontal) the incoming light is circularly polarized. The backscattered beam, in general, consists of a left- and a right-hand circularly polarized part, which on passing back through the $\lambda/4$ wave plate is converted into linear polarization. The corotating part is now vertically polarized, the contraroting part horizontally (the circular polarizations are specified in the lab frame). Only vertically polarized light can pass the analyzer and is recorded. The intensities in the four different polarizations are then obtained by rotating the Fresnel rhomb and the $\lambda/4$ wave plate. Let us assume that the analyzer is vertical (*e.g.*, because of a higher sensitivity of the spectrometer for vertically polarized light), then the Raman polarizations are given by the settings in Table 7.4.

Figure 7.3 shows the Raman spectra of CCl_4 in (a) the two linear and (b) the circular polarizations. In this molecule the fully symmetric mode is characterized by only the isotropic invariant $\bar{\alpha}^2$ being different from zero. For the A_{1g} peak at $460\,\mathrm{cm}^{-1}$ a depolarization ratio $\rho = 0$ and a reversal coefficient $P = 0$ are expected; the other modes should show $\rho = 0.75$ and $P = 6$ ($\bar{\alpha}^2 = 0$, $\gamma_{as}^2 = 0$). All quantities are in excellent agreement with the measured values given in Fig. 7.3. Deviations from the theoretical value are usually found for the reversal coefficient, because the circular polarizations are much more affected by the non-ideal

Figure 7.3: Raman spectra of CCl_4 (a) under linear and (b) circular polarization. Next to the fully symmetric mode at $460\,\mathrm{cm}^{-1}$ and the mode at $314\,\mathrm{cm}^{-1}$ the measured depolarization ratio ρ and reversal coefficient P are given.
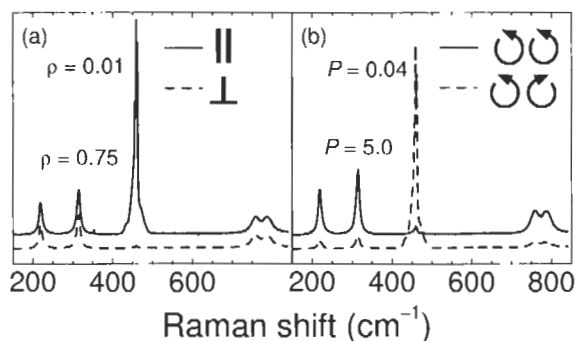
backscattering.[7.6],[7.23] While the theoretical depolarization ratio is the same regardless of the scattering geometry, the reversal coefficient, *e.g.*, in forward scattering, is the inverse of the backscattering value. In CCl_4 the measured P for the non-fully symmetric modes varies between 3.6 at 780 cm^{-1} and 5.3 at 220 cm^{-1}. A more robust indicator for the symmetry of a Raman mode than the raw values of ρ and P are the ratios between the tensor invariants. In particular, the ratio between the symmetric anisotropy and the isotropic invariant $\gamma_s^2/\bar{\alpha}^2 = 0.4$ for the 460 cm^{-1} mode, but $\gamma_s^2/\bar{\alpha}^2$ is well above 100 for all other modes.

7.3 Raman Measurements at Large Phonon q

The Raman experiments commonly performed in laboratories and excited with laser light in the visible or near-visible energy regime are limited to Γ-point phonons in first order due to the small wave vector of the incident light. In backscattering geometry the maximal momentum transfer and hence phonon momentum is given by

$$q_{max} = \frac{4n\pi}{\lambda_i} \approx 0.01 \, \text{Å}^{-1}, \quad \text{say at } \lambda_i = 488 \text{ nm} \tag{7.21}$$

in a material with a refractive index $n = 4$. This is very small compared to the extent of the Brillouin zone in reciprocal space, for which the lattice constants set the relevant scale,

$$k_{max} = \frac{\pi}{a_0} \approx 1.3 \, \text{Å}^{-1}, \quad \text{say with } a_0 = 2.46 \, \text{Å as for graphite.} \tag{7.22}$$

There are several techniques of getting to larger wave vectors that have been used in the past. One is to create an artificial, smaller Brillouin zone by growing superlattices of different materials and studying the resulting $q \approx 0$ modes.[7.28],[7.29] In a way, this is happening in carbon nanotubes by wrapping up the graphene sheet and thus introducing Brillouin-zone folding, see also Sect. 2.1. Most of these new $q = 0$ modes in nanotubes are, however, forbidden by selection rules in first-order scattering. A second approach is to relax the perfect periodicity in single crystals. For example, the earliest reports of Raman scattering in graphite by Tuinstra and Koenig[7.30] showed that the now-called D mode arose from a defect-induced process at large q vectors; it is not allowed in the perfect crystal. Another example is the ion bombardement of crystalline silicon with Si atoms successively increasing the damage to the material. In this way, one could show how the phonon density of states of a-Si evolved from that of c-Si.[7.31] The partially oxygenated high-temperature superconductor $YBa_2Cu_3O_{7-\delta}$ with δ around 0.3 shows defect-induced peaks at 230 and 600 cm^{-1}. Interestingly, the intensity of these defect peaks *decreases* when illuminated;[7.32],[7.33] light absorption *increases* the order of oxygen atoms in one of the crystal planes (the chain plane).

The optical Raman methods of large-q scattering, unfortunately, are connected with little specific information about the phonon dispersions. In second-order Raman scattering,[7.11],[7.34] for example, two phonons are emitted (or absorbed) at the same time, a process that is generally 10 to 100 times weaker than the first-order spectra. The momenta of the two phonons involved cancel for equal and opposite phonon vectors, and the condition $| \boldsymbol{q}_{max} | = | \boldsymbol{q}_1 - \boldsymbol{q}_2 | \approx 4n\pi/\lambda_i$ is easily fulfilled for visible light throughout the Brillouin zone. As a consequence, the Raman peak is an integration over the Brillouin zone, and regions with large densities of

Figure 7.4: Overbending in carbon nanotubes as function of chiral angle. The maximal overbending of a given tube in the range $2.8\,\text{Å} \le d \le 50.0\,\text{Å}$ was fitted to the empirical expression in Eq. (7.23), which is plotted here.
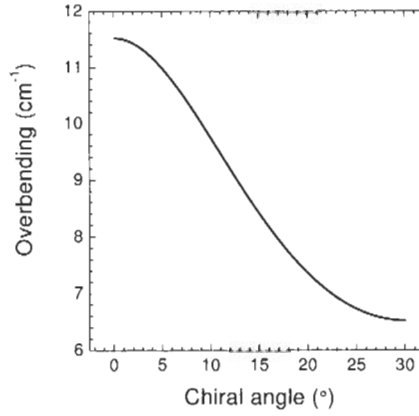
states become prominent in the spectra. Frequently this is near the Γ point, as the dispersion relations have zero slope there. In Si, *e.g.*, the second-order peak at $1000\,\text{cm}^{-1}$ arises from the optical phonon branch of Si, see the density-of-states calculation of Weber.[7.35] The 2nd-order peak goes to zero at $1040\,\text{cm}^{-1}$, a frequency twice the highest LO frequency at the Γ point, which is $521\,\text{cm}^{-1}$.

The situation is different when the Γ point is not the maximum in the phonon dispersion, *i.e.*, when it is a minimum or a saddle point. Then a second-order Raman peak at more than twice the highest first-order frequency appears in the spectra. This is the case in graphite,[7.36] diamond,[7.37],[7.38] and possibly AlSb.[7.39] The frequency of this peak, divided by two, corresponds to the maximum in the dispersion curves. We refer to the maximum phonon frequency being higher than the frequency at the Γ point as *overbending*. The reproduction of this phenomenon in lattice dynamical calculations is considered a stringent quality test of the calculation. Recent *ab-initio* work on diamond[7.40] and graphite[7.41],[7.42] and AlSb[7.43] have confirmed these overbendings. Since the dispersion of graphite shows an overbending, the question is what happens to the 2nd-order or even the 1st-order spectrum in carbon nanotubes.

In a symmetry-based study of the phonon dispersion of nanotubes with over 1000 different chiralities with a modified force-constants model, Dobardžić *et al.*[7.44] found the overbending empirically to depend on chirality as

$$\Delta E(\theta) = -1.158 + \frac{9.57}{1 - 0.245 \cos 6\theta} \quad (\text{in cm}^{-1}), \tag{7.23}$$

where ΔE is defined as the energy difference between the local band minimum at $\boldsymbol{q} = 0$ and the highest point in the dispersion and is given in cm^{-1}. They also give an expression for the $\boldsymbol{k}$ point at which the maximum occurs. Note that as a function of chiral angle the overbending drops from its largest value for zig-zag tubes to about half that for armchair ones. *Ab-initio* calculations confirm the overbending also for carbon nanotubes.[7.41],[7.45]

An experimental 2nd-order spectrum is shown in Fig. 7.5. It is seen that the frequency difference between the two peaks in the graphite traces has disappeared in single-walled nanotubes;[7.34] which has been interpreted as an overall softening of the lattice vibrations by about

Figure 7.5: 2nd-order Raman spectrum of single-walled and multiwall nanotubes and graphite in comparison (noise trace, upper scale). The less noisy trace is the first-order Raman spectrum (lower scale), the two scales differ by a factor of two. The vertical lines indicate the Γ-point frequency of graphite and the maximum in the dispersion from overbending. After Ref. [7.34].
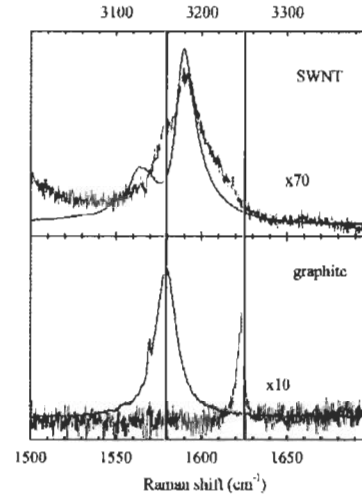
$30\,\text{cm}^{-1}$. On the other hand, the maximum of the SWNT first-order peak is higher than that of the graphite peak by at least $10\,\text{cm}^{-1}$, which indicates a hardening of the lattice.

The hardening of Γ-point phonons in nanotubes is one possible interpretation of the shift of the first-order phonon. An alternative explanation is based on a process that allows large-*q* scattering in optical experiments by a double-resonance process. Then the increase in Raman frequency in tubes is due to the larger *q*-vector involved in the double resonance and hence, if overbending is present, a larger frequency appears in the Raman spectrum. When treating the vibrations of carbon nanotubes in the zone-folding approximation, it is important to know whether or not there is overbending, as eigenmodes other than the fully symmetric ones correspond to $q > 0$ in the graphite Brillouin zone. See also Chap. 2 for a discussion of the zone-folding approximation and Sect. 8.5 for the interpretation of the high-energy mode in single-walled nanotubes. The double-resonance process is explained in Sect. 7.4.

Finally, we mention a new method for measuring the full phonon dispersion of tiny crystals too small for neutron scattering experiments. With a highly focused synchrotron radiation beam (spot size $30 \times 60\,\mu\text{m}$) it has become now nearly routinely possible to investigate the full Brillouin zone of solids. The technical breakthrough was made possible by the brightness of the new synchrotron light sources and by high-order, temperature-controlled Si-crystal-based X-ray monochromators. At an incident photon energy of about $20\,\text{keV}$ these monochromators operate with an energy resolution of 3 meV or about $20\,\text{cm}^{-1}$ (full width at half maximum of the Raman peaks). The first such measurements on diamond were reported by Schwoerer-Böhning *et al.*,[7.38] others followed by investigating GaN.[7.46] We show in Fig. 7.6 the dispersion obtained for the high-energy modes of graphite, because they play an important role in the wide spread zone-folding approach to nanotubes.[7.42] In the past, force-constants and *ab-initio* calculations have given large qualitative and quantitative differences in slopes, frequencies and crossings of the TO- and LO-related phonon branches. None of the calculations existing before the measurements had predicted correctly all aspects, see, *e.g.*, Refs. [7.41], [7.47] and [7.48]. The open symbols with the spline-extrapolated lines are
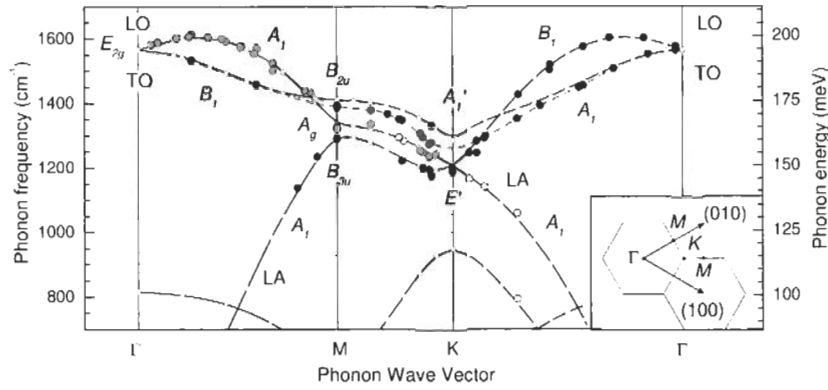
Figure 7.6: Phonon dispersion relations of graphite. Clearly seen is the overbending of the LO branch in both ΓM and ΓK-directions. Note also the crossing of the LO and TO branch between Γ and M. The measurements were taken by inelastic X-ray Raman scattering, the calculation was performed *ab initio*. From Ref. [7.42].

ab-initio calculations performed by Maultzsch *et al.*,[7.42] who found that taking into account the long-range nature of the dynamical matrix was mostly responsible for the much improved agreement between theory and experiment (Fig. 7.6). Only the calculated TO-related branch near the K-point shows a slight deviation from experiment.

We showed that while large-q Raman methods are available, most practical applications of Raman scattering in solids, however, are restrained to small-wave vector experiments for the time being. An exception occurs in carbon nanotubes: due to the particular electronic band structure their Raman spectrum is dominated by so-called double resonance processes, which do not have a general restriction to the Brillouin-zone center. We discuss this process now in more detail.

7.4   Double Resonant Raman Scattering

The Raman spectrum of graphite shows a number of different peaks besides the allowed E_{2g} Γ-point vibrations. The most prominent of them is the D mode around $1350\,\mathrm{cm}^{-1}$. This mode is induced by disorder; the weaker additional peaks appear because of disorder as well. It was found experimentally that the frequency of the disorder-induced modes depends on excitation energy. For example, the D-mode frequency increases by $50\,\mathrm{cm}^{-1}$ per 1 eV difference in laser energy. In Sect. 7.3 we saw that usually only $q = 0$ vibrations contribute to the first-order Raman spectrum. Therefore, the *frequency* of a Raman line is usually independent of the excitation energy. The shift of the D mode in graphite (and in carbon nanotubes) was very surprising and it took almost 20 years for its explanation.[7.49]

The mechanism responsible for the laser-energy dependence is defect-induced, double-resonant Raman scattering. The defect allows large phonon wave vectors q to contribute to the spectra; the double-resonance mechanism selectively enhances *specific* large-q modes. The observed frequency shift as a function of laser energy thus corresponds to the scanning

Figure 7.7: Non-resonant Raman scattering (a), single-resonant (b), and double-resonant scattering (c). The solid lines indicate real electronic states. The dashed lines represent virtual states, *i.e.*, energies that are not eigenenergies of the system. In the non-resonant process (a), both intermediate electronic states are virtual. If the laser energy matches a real electronic transition [first step in (b)], the Raman process is single resonant. When the special condition (c) is met, *i.e.*, in addition to (b) another electronic transition matches the phonon energy, the process is double resonant.
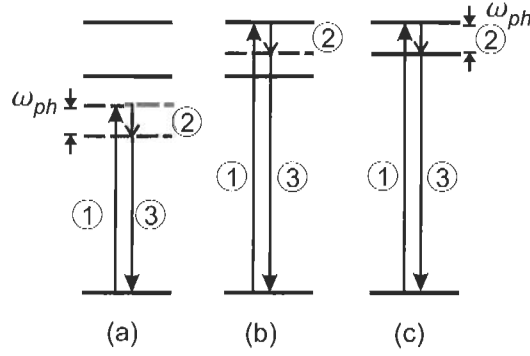
part of the phonon dispersion. Double-resonant Raman scattering evolved to be a key for understanding the Raman spectra of carbon nanotubes. Some aspects, however, are still under debate in the literature and are discussed in detail in Chap. 8. In this section we give an introduction to the concept of double-resonant Raman scattering.[7.3] We explain the characteristics of this effect, in particular the process that leads to a laser-energy dependence of the Raman frequencies in higher-order scattering.

We show in Fig. 7.7 a schematic view of non-resonant, single-resonant, and double-resonant first-order Raman scattering. The solid lines indicate real electronic states; the dashed gray lines denote virtual intermediate states. The incoming photon with energy E_1 excites an electron (1), the excited electron is scattered by emitting a phonon with energy $\hbar\omega_{ph}$ (2), and the electron recombines with the hole by emitting a photon with energy E_2 (3). If both intermediate states are virtual as in Fig. 7.7(a), the process is called non-resonant. If the laser energy matches the transition energy between two real electronic states [Fig. 7.7(b)], the Raman process is single-resonant. In this case, in Eq. (7.3) the first term in the denominator vanishes for $\gamma = 0$ and the Raman intensity diverges. To obtain double-resonant scattering, where two of the intermediate states are real [Fig. 7.7(c)], the electronic states must provide three suitable energy levels with energy differences equal to E_1, $\hbar\omega_{ph}$, and $E_1 - \hbar\omega_{ph}$. Experimentally, this rather restrictive condition can be fulfilled, if the electronic band structure of the material is tuned accordingly by applying uniaxial stress, an electric, or a magnetic field.[7.50]–[7.53] In semiconductor superlattices the intersubband transitions can be designed to match the required energy differences for the double-resonance condition.[7.54] In these examples, double-resonant scattering is obtained for only one particular wavelength of the incoming light.

In the above description of resonant and non-resonant Raman scattering, we restricted ourselves to first-order scattering that (for visible light) involves only Γ-point phonons. We extend the discussion now to higher-order processes, including scattering by two phonons of opposite wave vector or elastic scattering mediated by defects. In higher-order processes, the phonon wave vectors are not restricted to zero, see Sect. 7.3.

In Fig. 7.8 (a) two linear electronic bands are shown, which can be taken, *e.g.*, as an approximation to the graphene bands at the K point, see Chap. 3. Here, for any laser energy an incoming real transition is found. With increasing laser energy, the resonant transition oc-

curs at increasing electron wave vector $\boldsymbol{k}_i$. If the resonantly excited electron can be scattered by phonons with arbitrarily large wave vector $\boldsymbol{q}$, a second resonance is found for a particular phonon. Both energy and wave vector of this phonon are determined by the phonon dispersion and the double-resonance condition. The two resonant transitions that constitute the "double" resonance, are in our example the excitation of the electron by the incoming light and the inelastic scattering by the phonon. Because quasi-momentum is conserved, the process indicated in Fig. 7.8 (a) has to include the scattering by a second phonon ("second-order" Raman scattering) or by a defect (elastic scattering, shown here). In the case of defect scattering, the Raman matrix element is given by[7.3]

$$K_{2f,10} = \sum_{a,b,c} \frac{\mathcal{M}_{eR,\rho}\,\mathcal{M}_{e-def}\,\mathcal{M}_{ep}\,\mathcal{M}_{eR,\sigma}}{(E_1 - E_{ai}^e - i\gamma)(E_1 - \hbar\omega_{ph} - E_{bi}^e - i\gamma)(E_1 - \hbar\omega_{ph} - E_{ci}^e - i\gamma)}$$
$$+ \sum_{a,b,c} \frac{\mathcal{M}_{eR,\rho}\,\mathcal{M}_{ep}\,\mathcal{M}_{e-def}\,\mathcal{M}_{eR,\sigma}}{(E_1 - E_{ai}^e - i\gamma)(E_1 - E_{bi}^e - i\gamma)(E_1 - \hbar\omega_{ph} - E_{ci}^e - i\gamma)}, \quad (7.24)$$

where the notation is the same as in Eq. (7.3) and the matrix elements in the numerator are abbreviated as $\mathcal{M}_i$. $\mathcal{M}_{e-def}$ is the matrix element for the interaction between electron and defect. The first term in the sum describes the process, where the electron is first inelastically scattered by a phonon and second elastically by a defect; in the second term, the time order is reversed. For scattering by two phonons, Eq. (7.24) is modified accordingly.

We now inspect Eq. (7.24) in more detail. The sum over all possible intermediate electronic states a,b,c in Eq. (7.24) includes all non-resonant and single-resonant processes. The case $\boldsymbol{q} = 0$ is given if the electron wave vector $\boldsymbol{k}_b = \boldsymbol{k}_a$. This is illustrated in Fig. 7.8 (b), where some examples for single-resonant scattering with different phonon wave vectors and phonon frequencies are shown, including the process for $\boldsymbol{q} = 0$. The intensity of the single-resonant processes shown in Fig. 7.8 (b) is large, because one of the terms in the denominator of the Raman cross section vanishes. If for a particular combination of $\boldsymbol{q}$ and $\hbar\omega_{ph}$ the double-resonance condition is fulfilled, however, a second term vanishes and the Raman intensity is further increased. The double-resonant phonon mode is selectively enhanced and gives rise to a peak in the Raman spectrum. Only for laser energies below the first optical transition energy, *i.e.*, in non-resonant scattering, does the resulting Raman spectrum resemble the phonon density of states; such scattering is comparatively weak.

In Fig. 7.8 (c) we illustrate the effect on the Raman spectra when changing the incoming photon energy. As mentioned above, the electron wave vector $k_i = k_a$ at which the incoming resonance occurs is larger for higher laser energy. Consequently, the phonon that scatters the electron *resonantly* to a state $k_b = k_a - q$ must have a larger wave vector. This phonon will be enhanced and appears in the Raman spectrum. The Raman frequency of this mode is different from the frequency observed at smaller laser energy, depending on the phonon dispersion. Therefore, by changing the laser energy one can, in principle, measure the phonon dispersion. In general, this unusual dependence of Raman frequencies on the wavelength of the incoming light is a signature of double-resonant Raman scattering, if the process involves phonons with non-zero wave vector.

So far in our examples the incoming light was in resonance with the electronic states (incoming resonance). Alternatively, the scattered light can be in resonance (outgoing resonance). We show in Fig. 7.9 (upper row) the four processes resulting from the two time orders
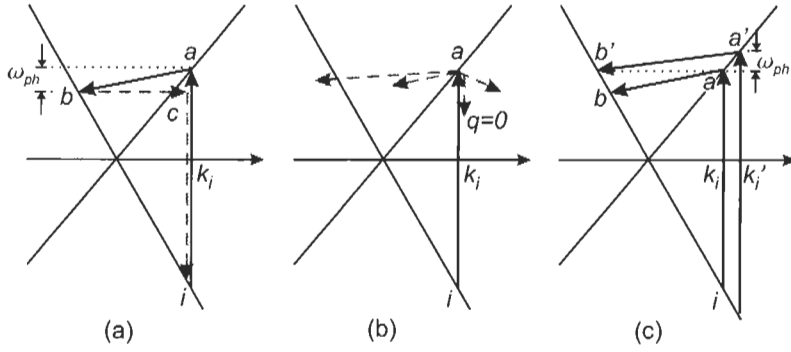
Figure 7.8: (a): Double-resonant Raman scattering at two linear electronic bands as, *e.g.*, at the *K* point in graphene. Resonant (non-resonant) transitions are indicated by solid (dashed, gray) arrows. The incoming light resonantly excites an electron at wave vector k_i. The electron is resonantly scattered by a phonon from state a to b. From b the electron is elastically scattered back to c (with $k_c \approx k_i$) by a defect, where it recombines with the hole. The last two transitions are non-resonant. (b): Examples of single-resonant scattering, where only the first transition is resonant. The excited electron is non-resonantly scattered by phonons with different wave vectors, including the case $q = 0$. (c): Double-resonant scattering at two different laser energies. The double-resonant phonon wave vector and hence frequency depend on the incoming energy. In (b) and (c) the last two transitions are omitted for simplicity, *i.e.*, elastic scattering by the defect and recombination of the electron and hole.

in Eq. (7.24) and incoming/outgoing resonance. Moreover, in the case of different electron and hole dispersions, the analogous processes have to be taken into account, where the hole instead of the electron is scattered. Finally, if the bands are not symmetric with respect to the minimum, the contributions depend on whether the optical transitions occur on the left or on the right of the minimum. All processes shown in Fig. 7.9 (a)–(d), however, are contained in Eq. (7.24), if the sum is taken over all intermediate states.

We will now evaluate the first term in Eq. (7.24) for the configuration shown in Fig. 7.8, where two linear electronic bands cross the Fermi level at $k = 0$ with Fermi velocities $v_1 < 0$ and $v_2 > 0$. The differences in electronic energies are

$$E_{ai}^e = |k|(v_2 - v_1), \qquad E_{bi}^e \overset{k_i \leq 0}{=} -qv_1 \text{ or } \overset{k_i \geq 0}{=} qv_2, \text{ and } \qquad E_{ci} = |k|(v_2 - v_1). \quad (7.25)$$

The sum in Eq. (7.24) can be converted into an integral over the electron wave vector k in one dimension. Inserting the energies in Eq. (7.25) into the expression for the Raman cross section we obtain[7.3],[7.49]

$$K_{2f,10} \propto \frac{(2\kappa_2 - q)}{(v_2 - v_1)^3 \left(\kappa_2 - q\frac{v_2}{v_2 - v_1}\right)\left(\kappa_2 + q\frac{v_2}{v_2 - v_1}\right)} \int_0^\infty \frac{dk}{(\kappa_1 - k)(\kappa_2 - k)}. \quad (7.26)$$

Here we assumed the matrix elements in the enumerator of Eq. (7.24) to be constant. The integral is straightforwardly evaluated and yields

$$K_{2f,10} \propto \frac{b}{\left(\kappa_2 - q\frac{v_2}{v_2 - v_1}\right)\left(\kappa_2 + q\frac{v_1}{v_2 - v_1}\right)}, \quad (7.27)$$
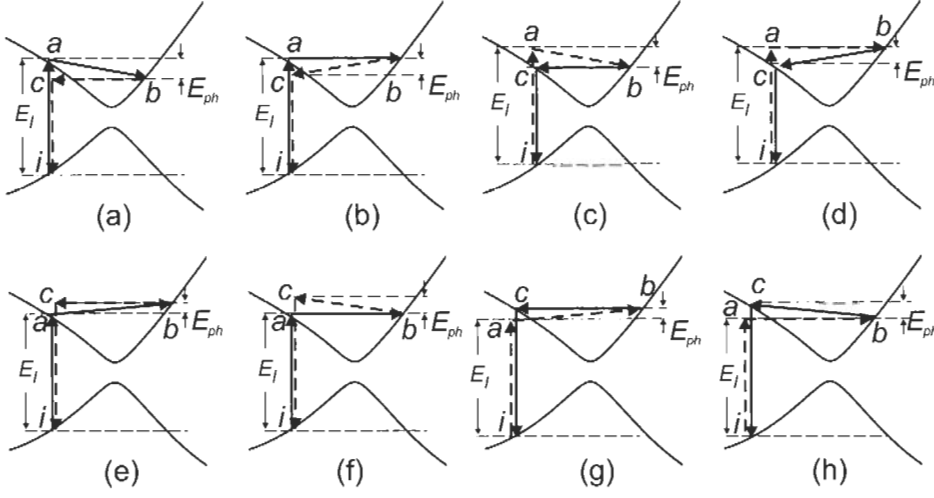
Figure 7.9: Double-resonant processes for Stokes (a-d) and anti-Stokes (e–h) scattering. Solid and dashed arrows indicate resonant and non-resonant transitions, respectively. In each row, the first two pictures show an incoming resonance; the last two pictures show an outgoing resonance. In (a) [and from here in every other picture] the electron is scattered first inelastically by a phonon and second elastically by a defect. This time order is reversed in (b).

where b is a slowly varying function of q

$$b = \ln(\kappa_2/\kappa_1)(2\kappa_2 - q)/[(v_2 - v_1)^2 \hbar \omega_{\mathrm{ph}}],$$

and

$$\kappa_1 = (E_1 - i\hbar\gamma)/(v_2 - v_1) \quad \text{and} \quad \kappa_2 = (E_1 - \hbar\omega_{\mathrm{ph}} - i\hbar\gamma)/(v_2 - v_1).$$

A double resonance occurs for those combinations of phonon wave vector q and energy $\hbar\omega_{ph}(q)$, for which one of the terms in the denominator of Eq. (7.27) vanishes.[7.3] Here the first and second terms correspond to incoming and outgoing resonance, respectively. The denominator vanishes for the double-resonant phonon wave vectors

$$q = \frac{E_1 - \hbar\omega_{ph}(q)}{v_2} \quad \text{and} \quad q = \frac{E_1 - \hbar\omega_{ph}(q)}{-v_1}. \tag{7.28}$$

In the approximation of $\hbar\omega_{ph} \approx 0$ and symmetric electron bands, we can simplify this condition to the so-called $q = 2k$ rule, *i.e.*, the double-resonant phonon wave vector is given by twice the wave vector of the excited electron. This is correct if the defect is involved in a resonant transition as for instance shown in Fig. 7.9 (b) and (f), and if $v_1 = -v_2$. This rule is a good approximation for estimating the double-resonant phonon wave vector. It cannot, however, substitute the full integration of the Raman cross section in Eq. (7.24) when deriving precise phonon frequencies or calculating a Raman spectrum.
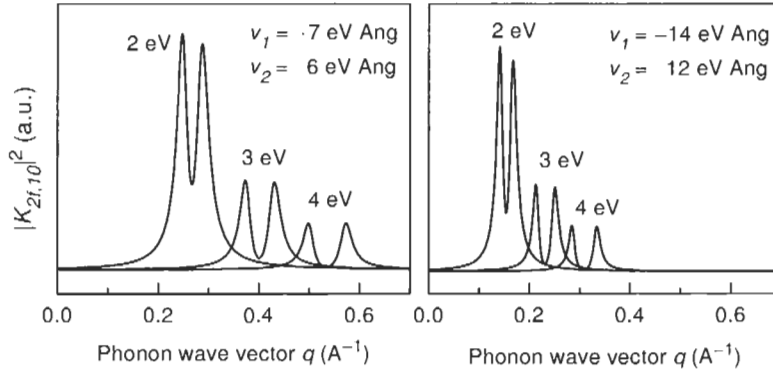
Figure 7.10: Raman intensity as a function of the phonon wave vector for laser energies between 2 and 4 eV, calculated from Eq. (7.27) for linear electronic bands. On the right, the slope of the electronic bands is doubled; the shift of the Raman peaks with laser energy is therefore smaller by a factor of two. We used a linear phonon dispersion and a broadening $\gamma = 0.1$ eV.

In Fig. 7.10 we plot the Raman intensity, as a function of q for different laser energies. We chose $\hbar\omega_{ph}$ to depend linearly on q; the Raman spectrum is obtained if the q-axis is transformed into $\hbar\omega_{ph}$.[2] We see in Fig. 7.10 the clear dependence of the selected phonon wave vectors and hence the Raman frequencies on excitation energy. The double-peak structure is due to incoming and outgoing resonance. Because of the linear electron and phonon dispersion, the shift with laser energy is linear as well. The effect of the electronic bands on the laser-energy dependence is shown in Fig. 7.10 (b), where the electron Fermi velocities were doubled. Now the same change in laser energy results in a smaller change in the electron wave vector k_i of the resonant optical transition. Therefore, the double-resonant phonon wave vector is less affected as well. Again, as the dispersion relations are linear in our example, the shift of the Raman peaks with laser energy decreases by a factor of two when the slope of the electronic bands is doubled. It is obvious that a larger phonon dispersion results in a more pronounced laser-energy dependence of the Raman spectra.

Besides the laser-energy dependence, another unexpected result was obtained for the D mode in graphite. For the same laser energy, Stokes and anti-Stokes spectra are different.[7.55] We illustrate in Fig. 7.9 (lower row) that this behavior, too, follows naturally from double-resonant scattering. The double-resonance condition is different for absorption and emission of a phonon at a given excitation energy. In the example shown in Fig. 7.9, the phonon wave vector is larger in anti-Stokes than in Stokes scattering. This can be seen by comparing, for instance, Fig. 7.9 (a) and (e). For anti-Stokes scattering, the sign of the phonon energy in Eq. (7.24) has to be inverted.

For second-order scattering, the elastic scattering by a defect is replaced by inelastic scattering by a second phonon. In the case of two phonons with the same frequency but opposite wave vector, the Raman shift is about twice the single-phonon (first-order) frequency and hence the shift with laser energy is approximately doubled. Because the quasi-momentum

---

[2]This is trivial for a linear phonon dispersion. Otherwise the phonon density of states has to be taken into account.

Figure 7.11: Raman spectra of Ge at different laser wavelengths. The Raman peaks result from double-resonant Raman scattering of overtones and combinations of acoustic phonons with large wave vector q. The peaks show a large upshift with increasing laser energy. From Ref. [7.56].
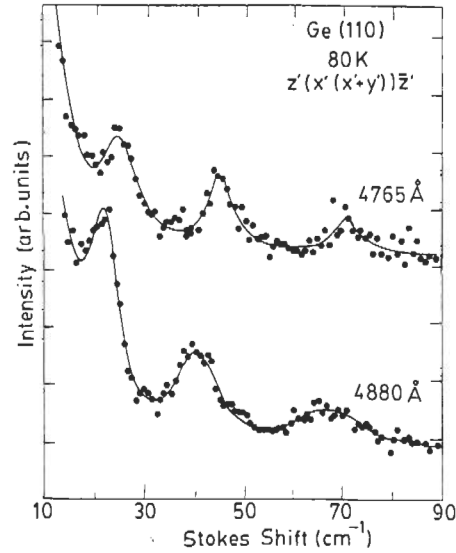
conservation can always be fulfilled for scattering by two phonons, the second-order spectrum can be double-resonant, independently of the presence of defects. As an example, we show in Fig. 7.11 the low-frequency Raman spectra of germanium at different laser wavelengths.[7.56] The peaks are due to scattering by two acoustic phonons with large wave vector q. The parabolic electronic bands give rise to double-resonant Raman scattering as shown in processes (a) and (c) in Fig. 7.9, where instead of the defect a second phonon is involved. Because the acoustic phonons are strongly dispersive, the Raman peaks in Fig. 7.11 shift with excitation energy.

The observed intensities of the Raman peaks are not solely determined by the double-resonance process. Those modes for which the double resonance takes place close to a singularity in the electronic density of states (Sect. 3.3), are further enhanced. This is easily understood from Eq. (7.24). For a given laser energy we sum over all possible intermediate states. At a high density of electronic states, more terms in the sum of Eq. (7.24) fulfill the first resonant condition and contribute to the second resonance as well. For the same reason, phonon modes from a region with a high phonon density of states contribute particularly strongly to the Raman signal. Therefore, the relative strength of these effects must be evaluated carefully.

The laser-energy dependence of the observed Raman frequencies constitutes the fingerprints of double-resonant Raman scattering with large phonon wave vectors. Stokes and anti-Stokes spectra are different for the same laser wavelength. Large phonon wave vectors are allowed in the case of higher-order scattering by two (or more) phonons or if defects are present in the sample, which relax the translation symmetry.

7.5   Summary

In this chapter we presented some basics of Raman scattering and its selection rules in as far as they are related to problems in carbon nanotubes. We showed how the symmetry of the Raman modes can be determined on unoriented samples from linearly and circularly polarized measurements and presented some methods used to study phonons with large q vectors. In the last section we explained the mechanism of double resonance which dominates the entire Raman spectrum of carbon nanotubes much more than in other solids. Many phenomena of the Raman spectra of carbon nanotubes can be explained quantitatively and qualitatively by double resonance, which is discussed in detail in Chap. 8.